Additive Manufacturing 35 (2020) 101411

Contents lists available at ScienceDirect

Additive Manufacturing

journal homepage: www.elsevier.com/locate/addma

Mechanical, thermal, and corrosion properties of Cu-10Sn alloy prepared by laser-powder-bed-fusion additive manufacturing

Congyuan Zeng[1], Bin Zhang[1], Ali Hemmasian Ettefagh, Hao Wen, Hong Yao, W.J. Meng, Shengmin Guo*

Department of Mechanical & Industrial Engineering, Louisiana State University, Baton Rouge, LA, 70803, USA

ARTICLE INFO

Keywords:
Cu-10Sn
Laser-powder-bed-fusion additive manufacturing
Thermal conductivity
Mechanical properties
Corrosion resistance

ABSTRACT

Cu-10Sn (wt. %) alloy specimens were prepared by Laser-Powder-Bed-Fusion based Additive Manufacturing (LPBF-AM). The compositions, microstructures, together with mechanical, thermal, and corrosion properties of LPBF-AM Cu-10Sn specimens were investigated in the as-fabricated (AF) condition and after vacuum annealing (VA) at 600 ℃ and 800 ℃. The AF specimens exhibit smaller grain sizes and higher compression strength than those of VA specimens, consistent with the Hall-Petch equation. Thermal conductivity of the AF specimens is around 10 % and over 20 % higher than that of the VA specimens annealed at 800 ℃ and 600 ℃, respectively, which can be ascribed to the two-phase constituents of the AF specimens. The corrosion rate of the AF specimens is almost two times higher than that of the VA specimens due to the differences in passive layer, intergranular corrosion, and internal galvanic corrosion.

1. Introduction

Cu-Sn alloys (tin-bronze) are used in a wide range of technological applications. For example, Cu-Sn (0–2 wt. % Sn) alloys are better chip interconnects than their Al-Cu counterparts due to the high activation energy for electromigration [1]; Cu-10Sn alloy is suited for making bearings due to its excellent mechanical properties, high thermal conductivity, as well as good wear and corrosion resistance [2]. Traditional methods for fabricating Cu-Sn alloy parts, such as casting and mechanical alloying, have been extensively studied [3,4]. However, the properties of Cu-Sn alloy parts made by additive manufacturing are less well known. One popular metal additive manufacturing method is laser-powder-bed-fusion based additive manufacturing (LPBF-AM), which uses a focused laser beam to melt and fuse metallic powders to form complex shaped parts with near full-density [5–7]. Due to the small size of the laser melt pool and high cooling rate, LPBF-AM parts possess phases and/or microstructures that are different from those formed in traditional processes, such as wrought and cast [5,8]. LPBF-AM has been used successfully to fabricate Cu-Sn alloy parts using Cu-4Sn alloy [9], Cu-4.3Sn alloy [10], Cu-10Sn alloy [11–13], Cu-15Sn alloy [14], and Cu-15Ni-8Sn alloy [15]. However, these Cu-Sn alloy AM studies mainly focused on microstructure characterizations and mechanical property evaluations.

For applications using Cu-Sn alloys, thermal and corrosion performances are as important as the mechanical properties. Thermal conductivity and corrosion behavior of traditional cast Cu-Sn alloys with varying tin contents have been extensively studied [16–22]. For example, thermal conductivity of cast Cu-Sn alloys show a significant dependence on Sn content and temperature, and increases as Sn content decreases and temperature increases [16]. Corrosion behaviors of Cu-Sn alloy parts manufactured with conventional methods are also well studied for different environments and Sn contents [17,21,23,24]. Two types of surface layers can be formed on Cu-Sn alloys after immersion in a corrosive environment. Type I is called noble patina, which consists mainly of a copper oxide on the surface as a protective layer. Type II is called vile patina, which involves the formation of a copper chloride layer [20,22]. To fill the knowledge gap regarding Cu-Sn alloy parts made by additive manufacturing, the present paper investigates the thermal and corrosion performances, together with mechanical properties, of Cu-10Sn alloy parts made by the LPBF-AM process.

2. Experimental procedures

2.1. Specimen preparation

Spherical Cu-10Sn alloy powders from Concept-Laser GmbH are

* Corresponding author.
E-mail address: sguo2@lsu.edu (S. Guo).
[1] Authors who have contributed equally to this article.

https://doi.org/10.1016/j.addma.2020.101411
Received 29 March 2020; Received in revised form 30 May 2020; Accepted 22 June 2020
Available online 24 June 2020

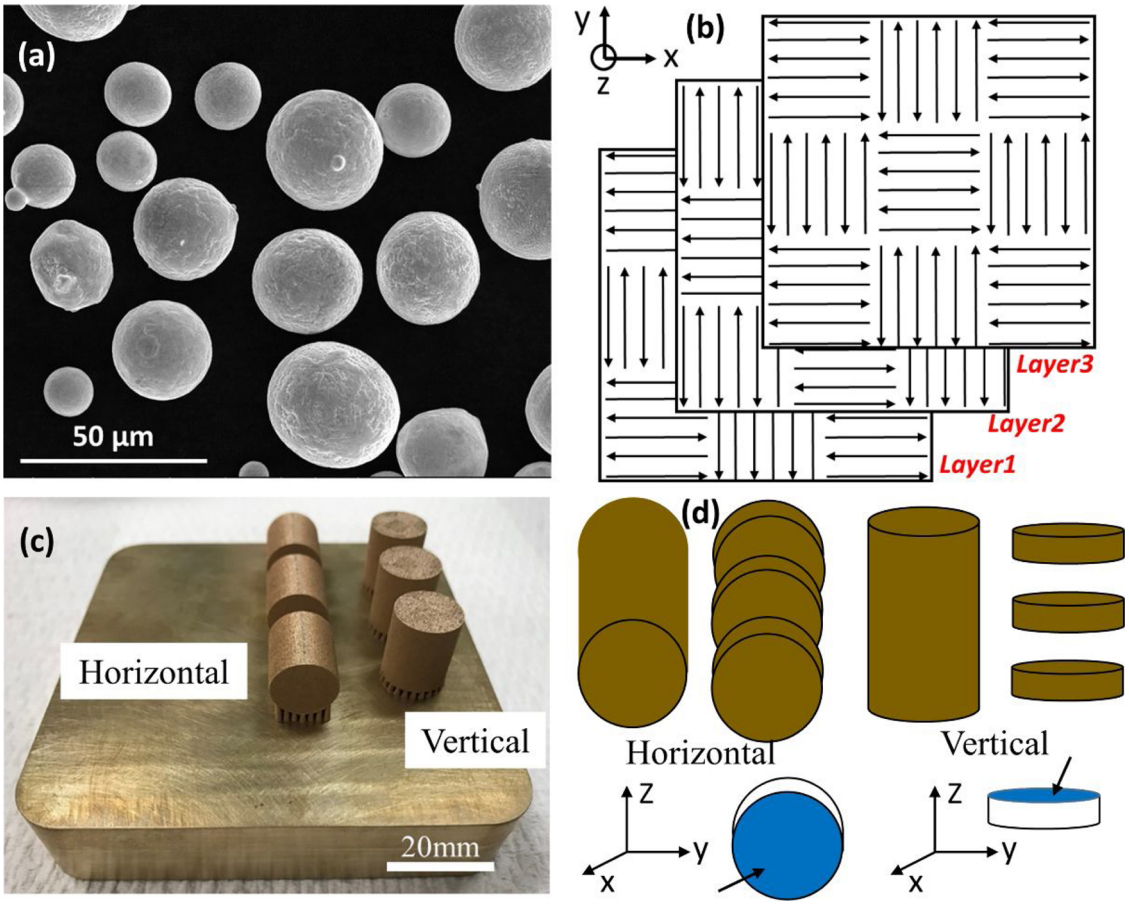

Fig. 1. (a): An SEM image of Cu-10Sn powders; (b): a schematic illustration of the laser "islands scanning strategy"; (c): as-fabricated cylindrical rod specimens built in the Vertical and Horizontal orientations; (d): a schematic illustration of Vertical and Horizontal specimens with shaded surfaces subject to subsequent microstructural characterization.

used in a LPBF-AM system (Concept-Laser Mlab cusing R) under the protection of Ar gas to fabricate the Cu-10Sn specimens. Fig. 1(a) shows the morphology of the Cu-10Sn powders. For size distributions, d10, d50, and d90 were determined to be 15.5 μm, 25.9 μm, and 37.6 μm, respectively, using Mastersizer 3000 (Malvern AERO S, dry powder dispersion mode). The LPBF-AM processing parameters are as follows: laser power 95 W, scanning speed 1200 mm/s, hatch space 50 μm, and powder layer thickness 15 μm. Laser "islands scanning strategy" is applied with a square island size of 5 × 5 mm^2 as shown in Fig. 1(b), where Axis Z represents the building direction.

In order to evaluate the influence of building direction on the mechanical, thermal and corrosion properties, two groups of cylindrical rod specimens were prepared, with the central axis oriented in either the Vertical or the Horizontal direction (Fig. 1(c)). Fig. 1(d) demonstrates the sectioning procedures for microstructural characterizations, thermal conductivity measurements, mechanical testing, and corrosion evaluation of AF and VA specimens. To investigate the effect of heat treatment on microstructural evolution and properties of LPBF-AM specimens, vacuum annealing is applied at $\sim 10^{-7}$ torr at temperatures of either 600 ℃ or 800 ℃ for 1 h. The programmed heating and cooling rates are both 10 ℃/min. In this paper, specimens are denoted by the combination of heat treatment conditions and the building orientations, i.e., AF-Horizontal, AF-Vertical, 600-Horizontal, 600-Vertical, 800-Horizontal, and 800-Vertical.

2.2. Testing procedures

Cylindrical rod specimens, 3.0 mm in diameter and 4.0 mm in height, were cut out from the LPBF-AM parts for uniaxial compression testing. The top and bottom surfaces of each compression testing specimen were mechanically ground to a mirror finish, using SiC grinding papers of 320, 600, 800, 1000 and 1200 grits, sequentially. Three specimens for each orientation and heat treatment condition were tested on a MTS 858 testing system at room temperature using a custom built compression stage. Further details on the protocol for uniaxial compression testing can be found elsewhere [25].

Thermal diffusivity measurements were performed using a Netzsch LFA 467 H T HyperFlash®- light flash apparatus, which operated between room temperature and 1250 ℃. The LPBF-AM specimens had dimensions of Φ14 × 15 mm (Fig. 1(c)). For Thermal diffusivity measurements, thin disk specimens with dimensions of Φ12.56 × 2.55 mm were cut out using a wire electrical discharge machining (EDM) system, and the top/bottom surfaces of the disks were ground using SiC papers (320 and 600 grit, successively). Prior to the thermal diffusivity tests, the specimen density (ρ) was measured using Archimedes principle on both AF and VA specimens at room temperature. After cleaning with ethanol, the surfaces of the reference specimen (a pure copper material from NETZSCH corp.), and each target specimen were coated with a thin and uniform layer of graphite to ensure identical heat absorption. The thermal diffusivity (α) was measured directly using the LFA 467 apparatus between 25 ℃ and 250 ℃. Specific heat (C_p) was calculated after the measurements with the following equation,

$$C_{pr} \cdot m_r \cdot \Delta T_r = C_{pt} \cdot m_t \cdot \Delta T_t \quad (1)$$

where m is the mass of the specimen, ΔT is the maximum temperature rise of the specimen during individual flash light shot; Subscripts and t indicate the reference and tested specimens, respectively. With the already known C_p of the reference specimen, C_p of the tested specimens

can be determined. At each testing temperature, at least three measurements were carried out. Thermal conductivity (K) was then be calculated following the equation below.

$$K = \alpha \bullet C_p \bullet \rho \quad (2)$$

To evaluate the corrosion performance, a 3-electrode standard corrosion cell was utilized to perform the electrochemical tests, using a saturated calomel electrode (SCE) as the reference electrode, a platinum counter electrode, and the specimens as the working electrode with an exposed area of 1.13 cm^2. Corrosion tests were conducted in 3.5 wt.% NaCl water solution at room temperature with naturally dissolved oxygen using a CHI-604C corrosion tester (CH Instruments, Inc). Open circuit potential (OCP) was recorded for a duration of ~60 h and Tafel curves were obtained within the potential range of -1.5 VSCE to 0 VSCE at a scan rate of 1.67 mV/s. Prior to the corrosion tests, the specimen surfaces were prepared by grinding with SiC paper (grit sizes 320, 600, 800 and 1000 in sequence), rinsing, and soaking in the test environment for 1 h. To ensure the reproducibility of the tests, all of the corrosion tests were performed at least three times. For weight loss test, all the polished specimens were washed by deionized water, ethanol, and acetone, and weighed after drying. Specimens were then hung in the solution for 11 days and the weight of corroded specimens was tracked every 24 h. Prior to weighing, specimens were cleaned and dried.

2.3. Materials characterization

3D visualizations for determining the size and distribution of internal porosity were conducted using a ZEISS X-ray micro-CT system (Xradia 620 Versa). Cubic AF-Horizontal and 800-Horizontal specimens were examined with a 3 mm × 3 mm field of view and 160 kV/25 W of energy/power. A voxel size of 1.5 μm was utilized for the characterization.

Phase identifications were carried out using X-ray diffraction (XRD) on both AF and VA specimens, as well as on the Cu-10Sn powders. θ-2θ scans were conducted in the angular range of 20°-120° 2θ with a scanning step size of 0.026°. XRD Rietveld refinement was also carried out with the FullProf package to estimate the quantitative phase constituents of the AF specimens. A fifth order polynomial function was utilized to model the background, a pseudo-voigt algorithm was used to fit the peak shape, and a least square refinement was applied to model the refinement weighting. Refinement was performed until a close fit between the experimental and calculated patterns was achieved.

An FEI Quanta3D FEG Dual-Beam scanning electron microscope/focused ion beam (SEM/FIB) instrument, with an electron backscatter diffraction (EBSD) attachment and an energy dispersive spectroscopy (EDX) attachment, was used for elemental analysis and microstructural examination of both AF and VA specimens. Prior to EBSD examinations, specimens were mechanically ground using SiC papers of different grit sizes (320, 600, 800, 1000 and 1200 grits, in sequence), polished with the MetaDi™ Supereme polycrystalline diamond suspension (6 μm, 3 μm, 1 μm, in sequence), followed by a final vibratory polishing with 50 nm silica suspension on a Pace Technologies GIGA 0900 Vibratory Polisher for 12 h. EBSD mapping was performed at 30 kV and 23 nA. Raw EBSD data were then analyzed with the TSL OIM software. After polishing, both AF and VA specimens were etched (5 g $FeCl_3$, 10 mL HCl, and 100 mL deionized water) at room temperature before SEM examination.

3. Results and discussions

3.1. Microstructure characterization

Fig. 2 shows XRD θ/2θ scans obtained from Cu-10Sn pre-alloyed powders, AF specimens, and VA specimens. The raw Cu-10Sn powders contain two phases which can be identified as the α-Cu(Sn) phase (a Cu-rich phase) and the intermetallic compound δ-$Cu_{40.5}Sn_{11}$ phase (a Sn-rich phase). After LPBF-AM processing, the phase compositions of both AF-Horizontal and AF-Vertical specimens are similar to those of the raw powders, i.e., both α and δ phases can be identified, consistent with other studies [11,14]. However, a closer examination reveals that the α phase diffraction peaks in AF specimens shift towards smaller angles as compared to those in the pre-alloyed powders. For example, as shown in Fig. 2(b), the (111) peak of α phase in AF-Horizontal specimen is 42.87°, slightly smaller than that of raw powders (43.01°). This shift of α phase peak to a lower angle suggests Sn diffusion into the α phase during the LPBF-AM process. After annealing, all the specimens contain only the α phase (Figs. 2(a) and 2(b)), indicating that Cu and Sn are mixed homogeneously after annealing at 600 °C/800 °C for 1 h. It is also clear that the diffraction peaks from the annealed specimens became narrower than those corresponding to the AF specimens, implying compositional homogenization as well as grain growth. To determine the phase constituents of AF specimens, Rietveld refinement analysis of the XRD data obtained from AF-Vertical specimen was carried out, and shown in Fig. 2(c). The refinement results confirm that the XRD pattern of AF-Vertical Cu-10Sn specimen is fitted well when the phase constituents are assumed to be the face-centered cubic (FCC) α-Cu phase and the δ-$Cu_{40.5}Sn_{11}$ phase (weighted profile reliability factor, R_{wp} = 9.02 %), indicating a coexistence of the $Fm\bar{3}m$ α-Cu (Sn) phase and the $F\bar{4}3m$ δ-$Cu_{40.5}Sn_{11}$ phase at room temperature. And the content of the δ-$Cu_{40.5}Sn_{11}$ phase is estimated to be 25.9 wt.%.

Fig. 3 summarizes the SEM images obtained from the AF specimens after etching. Fig. 3(a) shows a typical melt pool profile, marked with dash lines, resulting from the LPBF-AM process. A closer examination reveals that the specimen microstructure is not uniform, and three different regions with distinct microstructures can be discerned, as marked with squares 1, 2, and 3 in Fig. 3(a). The region marked by square 1 is located at the intersection region of two adjacent melt tracks, and Fig. 3(b) shows the corresponding microstructure at higher magnification. Cellular structures can be observed, and these cellular structures consist of α phase (grey regions), and (α + δ) eutectoid phase (bright rings), consistent with previous observation [11,14]. During the solidification of the LPBF-AM process, α phase forms first (higher melting point), which acts as the cored dendrites, and from the center to the edges of the dendrites, Sn content gradually increases, making the formation of (α + δ) eutectoid phases possible according to the study of Mao et al. [14]. The widths of the bright rings are ~100 nm. Fig. 3(c) depicts the microstructure of region 2 in Fig. 3(a), in the center of a melt track. Again, the α phase matrix and the (α + δ) phase white rings can be observed. The average size of the structures in region 2 is much larger than that in region 1. Region 3 is located across the melt pool borderline, and columnar structures can be identified. These columnar structures are approximately aligned toward the center of the melt track, which is ascribed to the complex temperature gradients in the melt pool under LPBF-AM conditions. The spacing between columnar features is less than 1 μm. Similar microstructural morphologies were observed in LPBF-AM processed Cu-10Sn alloy [11] and Cu-15Sn alloy [14]. Fig. 3(e) and (f) illustrate the microstructures of an AF-Vertical specimen within the laser scanning plane, where laser tracks are evident. The width of each laser track is ~50 μm, consistent with the hatch space used in this work.

Fig. 4 illustrates the 3D visualization results, which depicts the sizes and distribution of pores inside the representative AF-Horizontal specimen (Fig. 4(a)) and 800-Horizontal specimen (Fig. 4(b)). Based on the measurements, pores are found distributing uniformly in both the specimens and the pores in the 800-Horizontal specimen are larger than those in the AF-Horizontal specimen. The porosities of the AF-Horizontal and 800-Horizontal specimens determined by the ZEISS X-ray micro-CT system are approximately 0.11 % and 0.33 %, respectively. Based on the bulk density examinations, the densities of the two specimens are almost identical (Table 2). Considering the voxel size used in the 3D visualization test was 1.5 μm, pores with the sizes much smaller than the voxel size would not be revealed clearly. Therefore, more

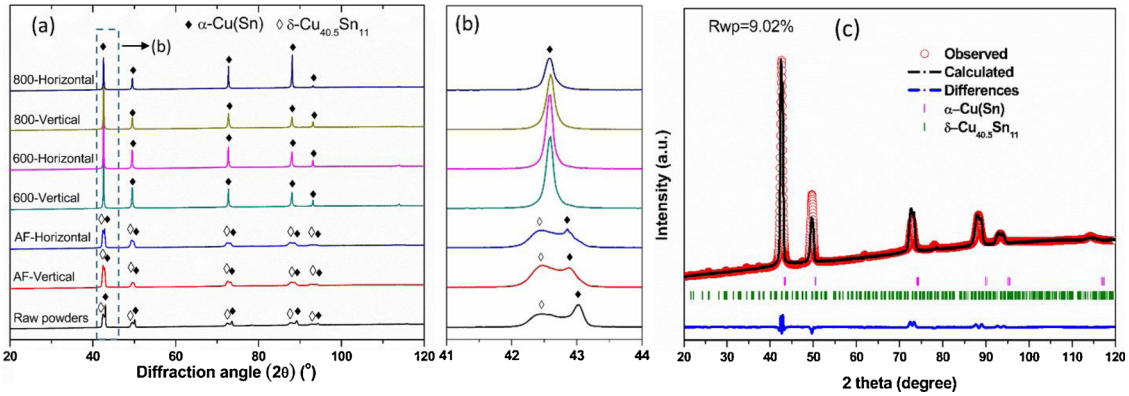

Fig. 2. XRD results and XRD Rietveld refinement analysis result: (a) θ/2θ diffraction patterns from the raw powders, AF and VA specimens over the 2θ range of 20°-120°; (b): θ/2θ diffraction patterns displayed over a narrower 2θ range of 41°-44°; (c) Rietveld refinement analysis of the AF-Vertical specimen.

nano-scale pores are likely to exist in the AF-Horizontal specimen. Fig. 4(c), (d), and (e) are the SEM images describing the pore sizes in the specimens. Clearly, with the increase of heat treatment temperature, the pore size increases.

Fig. 5 shows EBSD inverse pole figure (IPF) orientation maps of AF and VA specimens. Again, the mapped surfaces of the Horizontal specimens are parallel to the building direction (BD) (Fig. 5(a), (c) and (e)), while the mapped surfaces of the Vertical specimens are perpendicular to the building direction (Fig. 5(b), (d) and (f)). Fig. 5(a) shows the complex grain morphology for an AF-Horizontal specimen, with both elongated and equiaxed grains observed. The elongated grains are not aligned strictly along the building direction. This can be ascribed to the complex thermal gradients caused by the zigzag laser scanning directions and island laser scanning strategy employed in this work, and similar results can be found in LPBF-AM AlSi10Mg parts [17]. The elongated grains can be tens of micron in length and grow across several layers. Comparing Fig. 5(a) with Fig. 3(a)–(d), it is evident that the microstructures revealed by etching are not necessarily grains because of the apparent size difference between the etched structures and the mapped grains. Based on previous studies, the microstructures revealed by etching are actually subgrain structures, resulting from the insufficient diffusion of the alloying elements (i.e., Sn in the present study) due to the non-equilibrium solidification under a fast cooling condition, and are reported to be beneficial for improving the mechanical strengths of materials [26,27].

The average grain size, *d*, is estimated by the linear interception method using the TSL OIM software, and the value of *d* is ~2.1 μm for AF-Horizontal specimen. The small grain size is attributed to the high cooling rate associated with the LPBF-AM process. Fig. 5(b) presents the EBSD orientation map of an AF-Vertical specimen. The laser scanning tracks, as shown by the black dashed arrows, can be easily distinguished due to the fact that grains tend to grow towards the melt pool center. In addition, grains with different shapes can also be observed. The average grain size, *d*, of the AF-Vertical specimen is measured to be ~1.9 μm, close to its AF-Horizontal counterpart.

Fig. 5(c)–(f) summarize the EBSD IPF orientation maps of VA

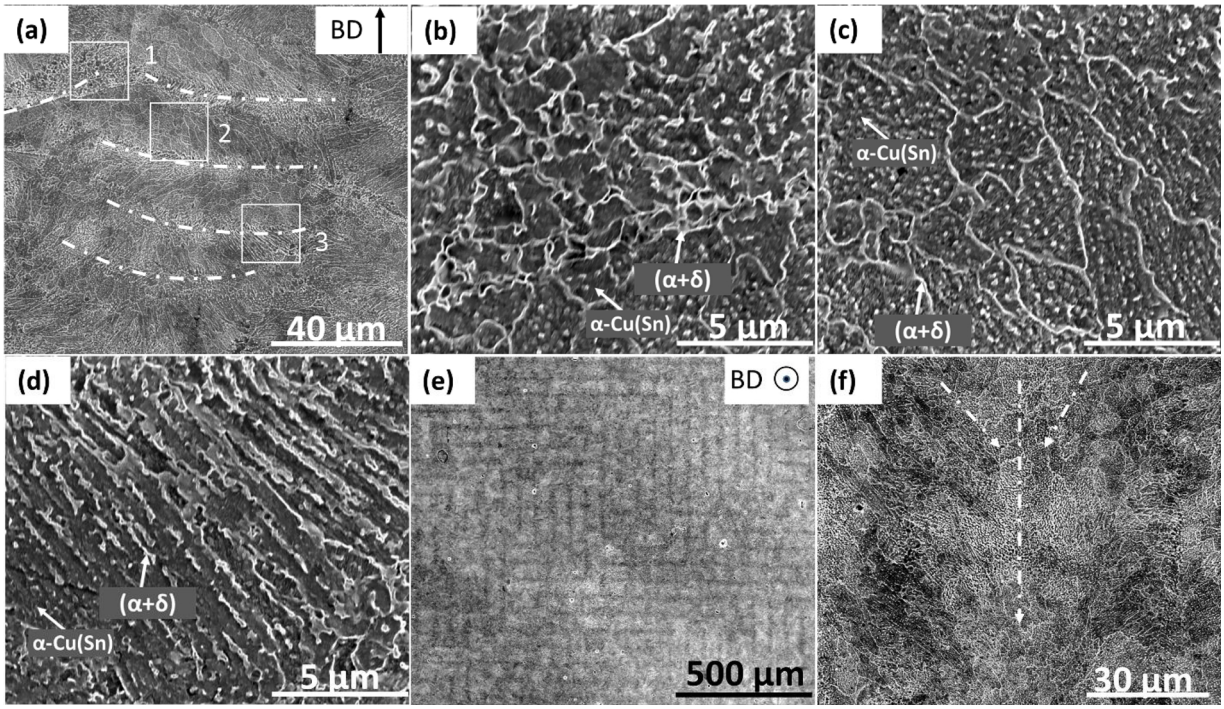

Fig. 3. Microstructural characterization of AF specimens. (a): AF-Horizontal specimen; (b),(c),& (d): SEM images of microstructures of area 1,2,3, respectively, marked as the white squares in (a); (e)&(f): SEM images of microstructures of an AF-Vertical specimen showing laser tracks with varying magnification. Arrows in (b), (c), (d) denote α and δ phase regions. Arrows in (f) denote the laser scan track direction.

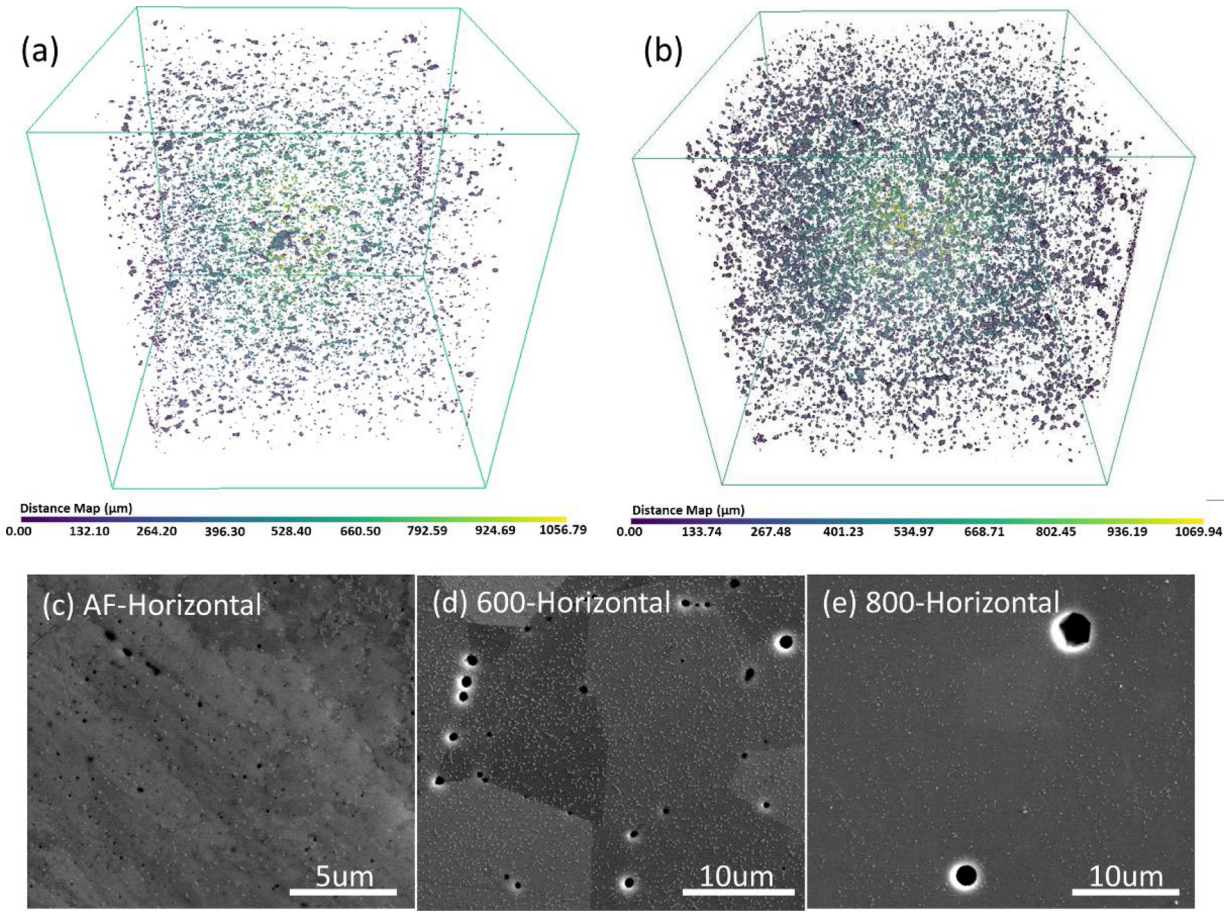

Fig. 4. Images showing the pore structures in the specimens. (a), (b) display the 3D visualization of pore structures for specimens AF-Horizontal and 800-Horizontal, respectively. (c), (d) and (e) are SEM images illustrating the pore sizes for specimens AF-Horizontal, 600-Horizontal and 800-Horizontal, respectively.

specimens. Clearly, grain morphologies have changed significantly after annealing, as compared to the AF specimens. After annealing, the grains are predominantly equiaxed, and an ample amount of twining can be observed within Cu-10Sn grains. Fig. 5(c) shows the grain morphology of a 600-Horizontal specimen. The presence of a small cluster of grains with sizes significantly smaller than the other grains may be a result of

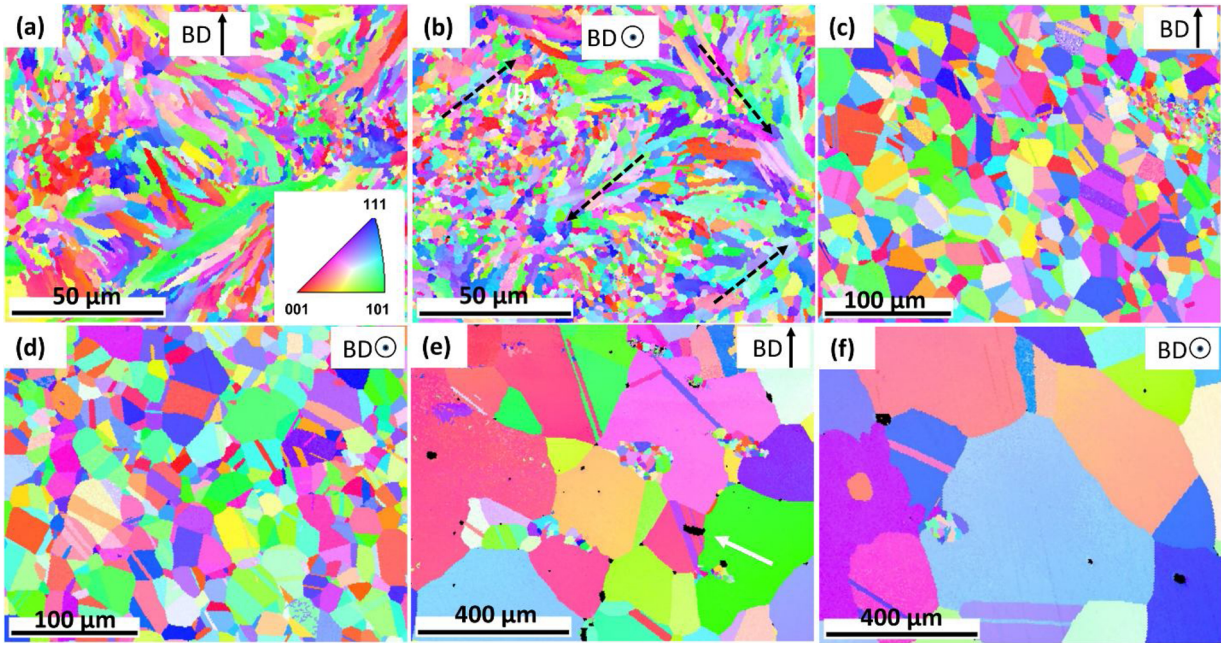

Fig. 5. Typical EBSD IPF maps of LPBF-AM Cu-10Sn specimens: (a) AF-Horizontal; (b): AF-Vertical; (c): 600- Horizontal; (d): 600-Vertical; (e): 800-Horizontal; and (f): 800-Vertical.

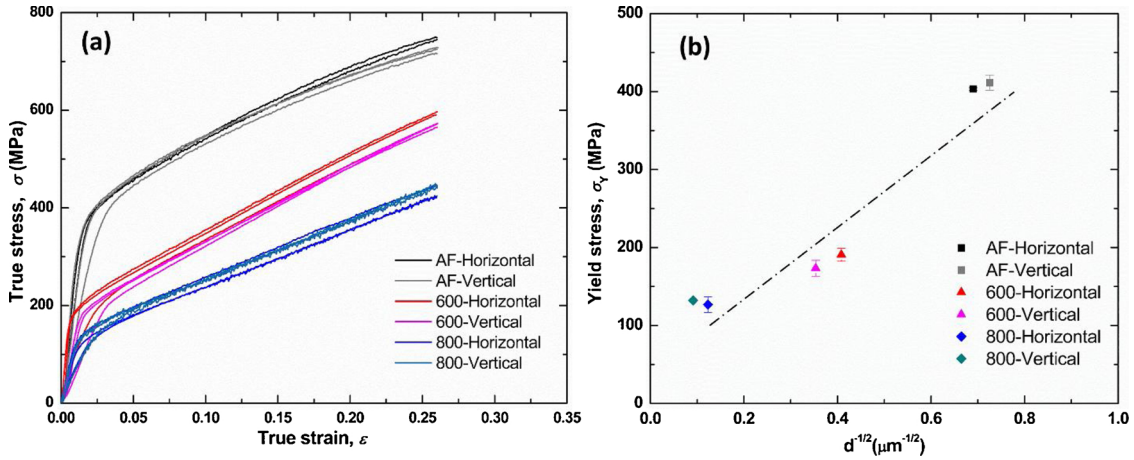

Fig. 6. Mechanical response of AF and VA Cu-10Sn alloy 3 mm diameter rod specimens. (a): true stress-true strain curves obtained from uniaxial compression testing; (b): plot of yield stress vs. the inverse square root of the average grain size.

insufficiently long holding time at 600 °C. The average grain size, *d*, is determined to be ~6 μm, including that portion of abnormally fine grains and intersection with twins. The average grain size of the 600-Vertical specimen, as shown in Fig. 5(d), is measured to be ~8 μm. After annealing at 800 °C for 1 h, dramatic grain growth was observed, as depicted in Fig. 5(e) and (f). Small clusters of finer grains are also observed, implying abnormal grain growth occurring in the annealing process. The average grain size, *d*, is calculated to be ~66 μm and ~120 μm for the 800-Horizontal and 800-Vertical specimens, respectively, again including the finer grains and twin intersections. The huge difference between the calculated average grain sizes of the 800-Horizontal and 800-Vertical specimens can be attributed to the existence of many more clusters of extremely fine grains in the former as compared to in the latter.

3.2. Mechanical response in uniaxial compression

Fig. 6 summarizes the true stress vs true strain (σ-ε) curves obtained from uniaxial compression tests on both AF and VA specimens. Even though the top and bottom surfaces of the rod specimens have been polished prior to compression, contacts between the top and bottom surfaces and the steel platens may still not be perfectly aligned, leading to early onset of plastic deformation localized at the contact regions. Consequently, the slope of the initial portion of the measured σ-ε curves are significantly lower than that corresponding to the theoretical elastic modulus for Cu-10Sn alloy. However, such mechanical misalignment effects diminish at larger strains, and the compression stress at larger strains are more reliable. It is clear that the AF specimens possess the highest compression strength, while the VA specimens exhibit lower strength values inversely related to the heat treatment temperature. It is also evident that the orientation of AF specimens has a minimal effect on the compression strength, and this can be attributed to the island laser scanning strategy used here. The anisotropy generated in LPBF-AM processed parts is the major drawback compared to wrought products, and the selection of laser scanning strategy can significantly influence the texture in the fabricated parts [28]. Compared to the standard raster scanning strategy, the island scanning strategy has been reported to reduce the texture index and improve isotropic properties of LPBF-AM AlSi10Mg parts [29] and LPBF-AM Inconel 718 parts [30]. The present compression tests indicate that the island scanning strategy can also be applied to produce Cu-10Sn AM parts to reduce the mechanical anisotropy. As shown in Fig. 5, the VA specimens consisted predominantly of equiaxed grains, and as expected, minimal effects of the initial specimen orientation were observed on the measured compression stress, as depicted in Fig. 6(a).

It is interesting to note that the measured σ-ε curves appear to exhibit linear strain hardening, i.e., within the strain range of $0.05 < \varepsilon < 0.25$, the measured true compression stress increases approximately linearly with increasing true compression strain. Thus, all the σ-ε curves within the strain range of 0.05 to 0.25 were fitted with a straight line of the form

$$\sigma = \sigma_Y + k\varepsilon \tag{3}$$

where k is a constant and σ_Y is the intercept on the stress axis. With this fitting, σ_Y was then taken as the yield stress. Fig. 6(b) plots the so-determined yield stress as a function of the inverse square root of the average grain size for both AF and VA specimens. The error bars on yield stress stem from averaging results of repeated compression tests. The apparent linear correlation between σ_Y and $1/\sqrt{d}$, as shown in Fig. 6(b), indicates that the compression yield stress of AF and VA specimens obeys the well-known Hall-Petch scaling, i.e., the yield stress correlates linearly with the inverse square root of the average grain size [31].

As shown in Fig. 6(b), the yield stress of the specimens annealed at the same temperature is nearly the same, indicating minimum effect of specimen orientation onto the mechanical properties after vacuum annealing, which is due to the generated equiaxed grain structures. The measured yield stress for the 800-Horizontal and 800-Vertical specimens is approximately 128.7 MPa, while for the 600-Horizontal and 600-Vertical specimens is around 179.4 MPa, close to the value corresponding to conventional cast parts [11,32,33] (Table 1). This observation is mainly attributed to the comparable grain sizes of the VA specimens with that of the cast counterparts from literature, i.e. several to several tens of microns [11,33]. The yield stress of AF specimens is ~411.9 MPa, about twice as high as the value reported previously of LPBF-AM Cu-10Sn parts [11] (Table 1). This value is even slightly higher than the best properties achieved in literature [12], where Cu-10Sn specimens were processed by varying laser intensity and the highest yield strength was obtained to be ~399 MPa. This improved yield stress of AF specimens is explained as follows. Laser energy density level (E) is described as the equation [12],

$$E = \frac{P}{v \cdot h \cdot t} \tag{4}$$

where P, v, h, and t are laser power, laser scanning speed, hatch space, and powder layer thickness, respectively. Based on the equation above, the laser energy density of the present study, reference [11] and [12] are 105.6 J/mm^3, 159.3 J/mm^3, and 220.0 J/mm^3, respectively. The laser energy density in reference [11] is between the other two studies. Therefore, the significantly reduced yield stress in the former is most likely ascribed to the much larger Cu-10Sn powders and medium laser energy density used, which is ~85 μm compared with ~60 μm in

Table 1
Comparison of mechanical properties and thermal conductivity of Cu-10Sn alloys prepared and treated with differing methods (from literature and present study).

Fabrication method	Mechanical property			Thermal conductivity (W/(m·K)) (25 − 250 °C)	Literature
	Yield stress (MPa)	Ultimate stress (MPa)	Elongation (%)		
Cast	154	248	/	/	[32]
Cast	172	252.52	18.29	/	[33]
Cast	120	220	7	/	[11]
HPS	123.4	216.5	12.5	/	[34]
HPS	210	586	23	/	[35]
ECAP	342.37	646.83	9.026	/	[33]
LENS™	153.2	/	/	46 − 69	[13]
LPBF	180	420	17	/	[11]
LPBF	399	490	19	/	[12]
LPBF	411.9 ± 10.1	/	/	43.6 ± 2.2–65.3 ± 1.8	Present study
LPBF + VA600 [a]	179.4 ± 7.8	/	/	35.4 ± 1.9–54.3 ± 2.4	Present study
LPBF + VA800 [b]	128.7 ± 10.1	/	/	39.3 ± 3.6–59.0 ± 3.9	Present study

[a] Specimen prepared with laser powder bed fusion, and vacuum annealed at 600 °C.
[b] Specimen prepared with laser powder bed fusion, and vacuum annealed at 800 °C.

Table 2
Densities of the specimens measured by Archimedes principle.

Specimen name	Density (g/cm^3)
AF-Horizontal	8.85 ± 0.056
AF-Vertical	8.88 ± 0.012
600-Horizontal	8.87 ± 0.008
600-Vertical	8.86 ± 0.032
800-Horizontal	8.85 ± 0.021
800-Vertical	8.83 ± 0.043

reference [12] and ~25.9 μm in the present study. More defects may exist in the specimen in reference [11] and deteriorate the yield strength. The slightly inferior yield stress in reference [12] compare with the AF specimens in this study is mainly attributed to the lager grain size (5.1 ± 1.8 μm) and negligible formation of δ phase, which acts as a reinforcement phase.

Several other fabrication methods and post treatment strategies have also been performed on Cu-10Sn alloys, i.e. hot press sintering (HPS) [34,35], laser engineered net shaping (LENS™) [13], equal channel angular pressing (ECAP) [33], and the corresponding mechanical and thermal properties are listed in Table 1. Apparently, yield stress of the specimens prepared or treated with the above three methods is lower than that in this study. In addition, specimen treated with ECAP method shows remarkably higher yield stress than the HPS/LENS™ methods prepared samples due to the significantly reduced grain size after severe plastic deformation [33]. However, the reduced grain size is still not comparable with that of the AF specimens in this study. Compared with LPBF process, LENS™ process has the feature of considerably larger laser energy input, leading to dramatically larger melt pool size and consequently much decreased cooling rate [36], which results in increased grain size, decreasing the mechanical strength due to the Hall-Petch effect. Similarly, the low mechanical strength of specimens made by HPS is also attributed to the low characteristic cooling rate, which is at the level of several tens of degrees per minute [37], much slower than that of the LPBF process (over 10^4 °C/min) [38]. Besides, eliminating voids inside the specimens remains challenging for the HPS process, i.e. voids existed around Cu_3Sn precipitates[34], detrimental to the overall mechanical performance. Table 1 also lists ultimate stress and elongation values of the specimens. In the present study, the preset testing strain limit was 25 %, clearly, no specimen failed at the strain limit, indicating superior ductility than the counterparts listed. Meanwhile, the stress of the AF specimens, VA specimens treated at 600 °C and 800 °C at the strain limit 25 % are 724.2 ± 13.8 MPa, 564.9 ± 12.6 MPA, and 426.6 ± 10.0 MPa, respectively. Again, greatly improved stress is observed in the AF specimens. The above comparison suggests that 1) LPBF-AM is a promising technique to make AM parts with high mechanical properties; 2) the LPBF-AM process parameters used in this paper were optimized for mechanical strength as compared to previously published work [11,12].

In addition to grain boundary strengthening, other factors, i.e., the formation of α-Cu(Sn) phase and fine (α + δ)-eutectoid, contribute to the good mechanical performance of LPBF-AM Cu10Sn specimens. The XRD results shown in Fig. 2 and the microstructures shown in Fig. 3 indicate that (α + δ)-eutectoid structures are dispersed throughout the α-Cu (Sn) phase, and that the size of (α + δ)-eutectoid structures is much smaller than that within cast parts due to the high cooling rates typical of the LPBF-AM process. Similar to a grain size effect where grain boundaries can hinder dislocation motion and the volume fraction of grain boundaries increases as the average grain size decreases, the dispersed fine (α + δ)-eutectoid structure can increase the density of α/(α + δ)-eutectoid interfaces. These interphase interfaces would also impede dislocation motion, leading to increase in mechanical strength. Besides, based on previous studies of Cu-4.3Sn part [10] and CM247LC Ni superalloy [39], the LPBF-AM process may induce high-density dislocations inside the as-fabricated components due to the non-equilibrium fast cooling process. Such dense dislocations further increase the mechanical strength of LPBF-AM parts. Last but not least, pores inside the specimens also influence mechanical properties. According to Table 2, densities of the specimens are quite similar, indicating close porosities. Based on the 3D visualization results and SEM images in Fig. 4, pore size increases with the increase of heat treatment temperature. It was reported that a decrease of pore size would improve the strength of the material by distributing the load more evenly [40–42]. Therefore, smaller pore size is probably another reason for the higher strength of the AF specimens.

3.3. Thermal conductivity evaluation

Table 2 lists the measured density values of both AF and VA specimens, which are very similar. These density values are used to calculate thermal conductivity based on the measured thermal diffusivity and the calculated specific heat values. Fig. 7 plots the so-determined thermal conductivity values for both AF and VA specimens versus testing temperatures. The error bars result from averaging the thermal conductivity values of repeated measurements. It is clear that all the curves are qualitatively similar, i.e., thermal conductivity values increase nearly linearly as temperature rises from 25 °C to 250 °C for both AF and VA specimens, consistent with previous studies [13]. However, it is also observed that AF-Vertical and 800-Vertical specimens exhibit slightly lower thermal conductivity values than those of AF-Horizontal

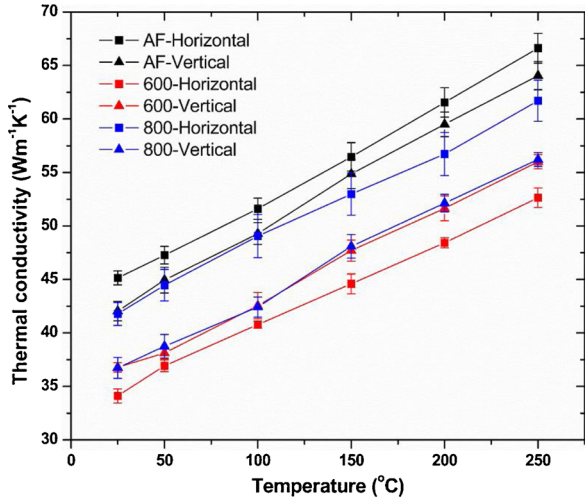

Fig. 7. Thermal conductivity of both AF and VA specimens vs. temperature.

and 800-Horizontal specimens, while the measured thermal conductivity values for 600-Vertical specimens are slightly higher than that of 600-Horizontal specimens, showing no clear influence of building orientations on thermal conductivity. The thermal conductivity values for AF specimens are approximately 10 % and over 20 % higher than those of specimens annealed at 800 ℃ and 600 ℃, respectively. The detailed thermal conductivity values are listed in Table 1. Thermal conductivity data from open literature for Cu-10Sn alloy are limited. The authors only identified one prior publication by Bhat et al. [13], who prepared Cu-10Sn alloy with the LENS process. Bhat et al. reported thermal conductivity from room temperature to 250 ℃, in good agreement with the AF specimens in this study.

For Cu-10Sn alloy, thermal conductivity can be divided into two main components, electronic thermal conductivity and lattice thermal conductivity, with heat carriers of electrons and phonons, respectively. Pores inside the specimens were reported to affect thermal properties by both the porosity and pore size [43]. In the present study, pores in the specimens influence thermal conductivity mainly by their sizes. Based on previous studies, when the pore size was decreased to be comparable with the mean free paths of electrons (~39 nm at room temperature [44,45]) and phonons or even smaller, electrons and phonons could be strongly scattered, reducing the electronic and phonon thermal conductivities [43,46]. Therefore, pores insides AF specimens could effectively decrease thermal conductivity due to their significantly smaller sizes in nano-scale. However, the observed thermal conductivity of the AF specimens is higher than the VA ones. Therefore, there must be another mechanism, which affects the thermal property dominantly.

According to the XRD results (Fig. 2(a)), AF specimens consist of two phases, a Cu-rich α phase and a Sn-rich δ phase, while VA specimens only have single α phase. To better understand the influence of these two phases on thermal conductivity of AF specimens, Fig. 8(a) plots thermal conductivity data available from the literature for Cu-Sn alloys (as-cast or annealed) at temperatures below 50 ℃ vs. the Sn content [16,47,48]. A least-squares fit to this data collection is shown as the red curve in Fig. 8(a), and can be expressed as

$$K = 233.37 \times (100 \times w_{Sn})^{-0.63} \tag{5}$$

where K and w_{Sn} represent thermal conductivity and Sn content of the Cu-Sn alloy, respectively. Eq. (5) can be applied to estimate thermal conductivity of single-phase Cu-Sn alloys. Extrapolating the fitted curve to the δ phase composition of 33.7 wt.% Sn yields an estimate for the thermal conductivity of the δ phase of 25.4 W/(m K). Considering Sn contents in specimens annealed at 600 ℃ and 800 ℃ are 8.3 wt.% and 8.2 wt.%, respectively, the estimated thermal conductivity for them are 61.5 W/(m K) and 61.9 W/(m K), respectively. Thermal conductivity of AF specimens can be estimated based on Maxwell's equation [49],

$$\frac{K_{eff}}{K_m} = 1 + \frac{3\varnothing}{\frac{K_l + 2K_m}{K_l - K_m} - \varnothing} \tag{6}$$

where K_{eff}, K_m and K_l represent respectively the effective thermal conductivity of the AF Cu-Sn alloy, α phase, and δ phase (K_m can be determined by Eq. (5)), and ∅ is the volume fraction of δ phase, which can be estimated using the following expression,

$$\varnothing = \frac{\frac{w_\delta}{\rho_\delta}}{\frac{w_\delta}{\rho_\delta} + \frac{w_\alpha}{\rho_\alpha}} \tag{7}$$

where ρ_α, ρ_δ are the densities of α phase and δ phase (8.68 g/cm^3 [50]), respectively, while w_α and w_δ represent the mass percentages of α phase and δ phase, and $w_\alpha + w_\delta = 1$. Assuming the specific volumes of Cu and Sn stay constant after the diffusion of the latter into the former, the following equation can be used to estimate the density of α phase,

$$\rho_\alpha = V_{Cu} \times \rho_{Cu} + V_{Sn} \times \rho_{Sn} \tag{8}$$

where ρ_{Cu} and ρ_{Sn} stand for the densities of Cu (8.96 g/cm^3) and Sn (7.31 g/cm^3), respectively, while V_{Cu} and V_{Sn} represent the volume fractions of Cu and Sn, and $V_{Cu} + V_{Sn} = 1$. The relation between the volume fraction of Sn, V_{Sn}, and mass content of Sn, w_{Sn}, in α phase can be expressed below,

$$V_{Sn} = \frac{\frac{w_{Sn}}{\rho_{Sn}}}{\frac{w_{Sn}}{\rho_{Sn}} + \frac{w_{Cu}}{\rho_{Cu}}} \tag{9}$$

where w_{Cu} is the mass fraction of Cu in α phase, and $w_{Sn} + w_{Cu} = 1$. Considering the Sn content in the AF specimens is 8.8 wt.%, the mass content of δ phase, w_δ, has a direct influence on w_{Sn}, which can be described as

$$w_{Sn} = \frac{0.337 w_\delta - 0.088}{w_\delta - 1} \tag{10}$$

Combine the expressions (5)-(10) above, it is evident that the thermal conductivity of AF specimens, K_{eff}, is also a functions of δ phase mass content, w_δ. Fig. 8(b) depicts the overall results. According to Fig. 8(b), when w_δ is 13 wt.%, K_{eff} is expected to be 75 W/(m·K), approximately 20 % higher than those of annealed specimens. This estimate is qualitatively consistent with the experimental observations shown in Fig. 7. The experimental observation of AF specimens possessing higher thermal conductivities as compared to VA specimens is due to a combination of factors: 1) the AF specimens contain both α and δ phases whereas the VA specimens contain only the α phase; 2) the thermal conductivity of the δ phase is substantially lower than that of the α phase; 3) the α phase Sn content in the VA specimens increases as the δ phase is dissolved within the α phase, leading to a decrease in α phase thermal conductivity.

Based on the Rietveld refinement of XRD results, w_δ is estimated to be 25.9 %, in which case, K_{eff} would be even higher. This discrepancy between the estimated and experimental thermal conductivity values of AF specimens is likely caused by the presence of defects within the specimens, including point defects, dislocations and grain boundaries, which can also strongly scatter phonons, leading to reduced lattice thermal conductivity of the materials [51].

3.4. Corrosion property

The weight changes of AF-Horizontal, 600-Horizontal, and 800-Horizontal specimens in a 3.5 wt. % NaCl water solution were recorded daily for 11 days (Fig. 9(a) and Table 3), which gave a measure of the relative corrosion rates. It is obvious that the corrosion rate of AF specimen is higher than that of the heat treated ones. According to data shown in Fig. 9(a), the corrosion performance of specimens vacuum

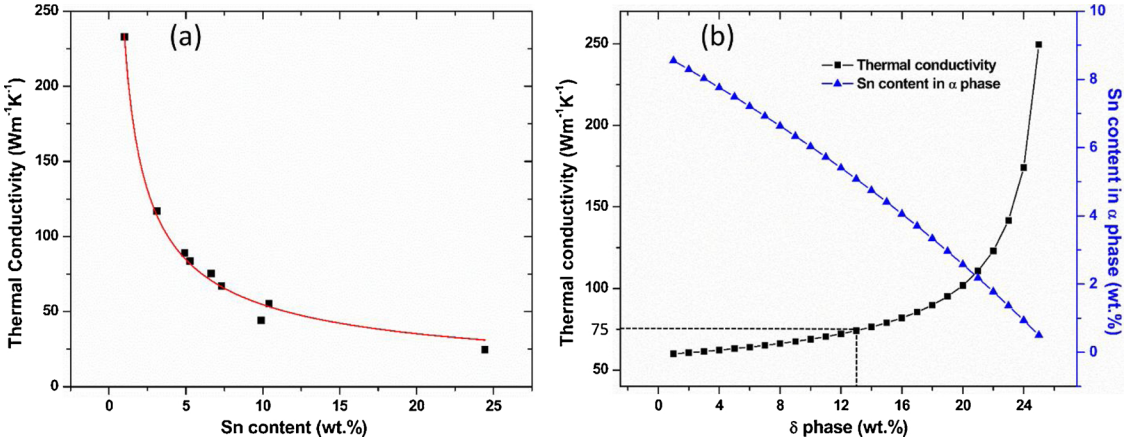

Fig. 8. (a) Thermal conductivity of Cu-10Sn ally vs. Sn content under 50℃ with a curve fitting. (c) The theoretically calculated thermal conductivity and Sn content in α phase as a function of δ phase content in AF specimen.

annealed at 600 ℃ and 800 ℃ was approximately the same. Fig. 9(b) presents θ-2θ XRD patterns obtained from AF and VA specimens after the weight loss test. The presence of a Cu_2O phase can be identified on all three specimen surfaces. The remaining peaks arise from the α phase and δ phase, as shown in Fig. 2. The absence of chloride compounds on the surface after the immersion test confirms the low aggressive corrosive environment and formation of noble patina (type I) on the surface.

Fig. 10(a) shows the change of specimens surface potential with time in an open circuit potential (OCP) test. It is clear that the curves are qualitatively similar for all three specimens, i.e., the potential decreases for the first couple of hours due to dissolution of pre-formed compounds on the surfaces, then the potential increases due to the formation of a protective layer (Cu_2O), and finally the potential reaches a steady state known as OCP. Minute fluctuations on the curves are a sign of precipitation and dissolution of the compounds during the reaction process between the specimens surfaces and the solution. Same as weight loss results, almost the same curves are obtained for the two VA specimens. However, the AF specimen has a more negative OCP value (~ -0.17 V) and needed a much longer time (30 h) for the surface to achieve the steady state as compared to the VA cases (~ -0.155 V and 8 h). It appears that the heat treatment process has a stabilizing effect on the formed passive layer by improving the passive layer quality and/or thickness.

Fig. 10(b) and Table 4 summarize the results of potentiodynamic polarization tests. As shown in Fig. 10(b), little difference is observed

Table 3
Slopes describing the weight loss rate of the AF-Horizontal, 600-Horizontal and 800-Horizontal specimens immersing in the solution for 11 days.

Specimen	Slope (mg/cm^2.day)	R^2
AF-Horizontal	0.612	0.98
600-Horizontal	0.469	0.96
800-Horizontal	0.466	0.96

for both VA specimens, while it is evident that the curve of AF specimen shifts to higher current densities and lower potentials compared to the VA specimens, indicating a more active surface and higher corrosion rate for the AF specimen. Specifically, as listed in Table 4, the corrosion current density of AF specimen is 7.586 μA/cm^2, over two times of the corrosion current density of the 800-Horizontal specimen, 3.236 μA/cm^2. The corrosion rate for both VA specimens are similar, consistent with the results from weight loss and OCP tests. In addition, all potentiodynamic curves have a region in the anodic branch where the current density is almost constant in the potential range of -0.2 ~ -0.35 V. This observation confirms the formation of a passive layer, which mainly consists of Cu_2O, as suggested by the XRD results shown in Fig. 9(b).

Intergranular corrosion is a localized form of corrosion, attacking along grain boundaries (GBs) due to the higher energy state of GBs as compared to the remaining parts of the surface. It is well known that an

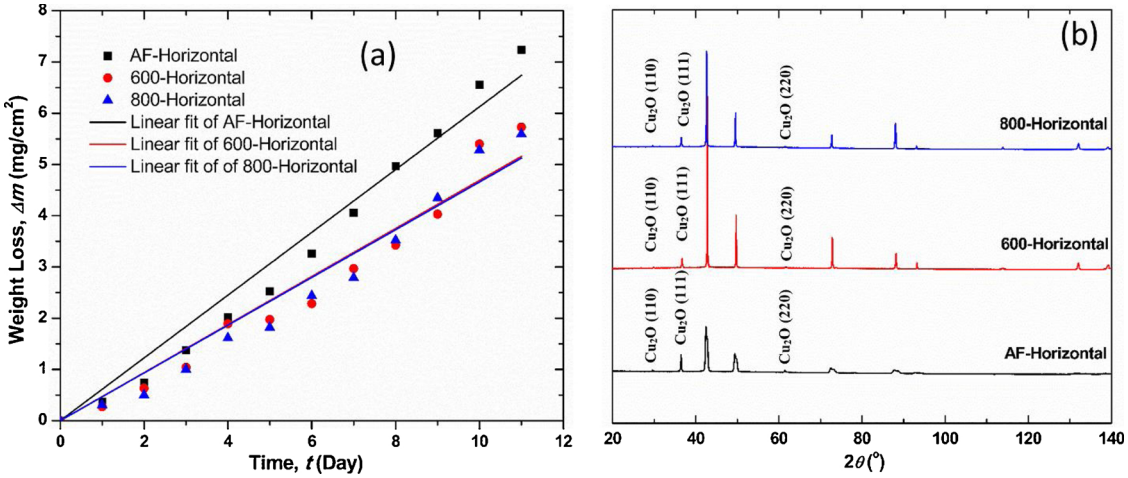

Fig. 9. (a) Weight loss test results of AF-Horizontal, 600-Horizontal, and 800-Horizontal specimens in 3.5 wt% NaCl water solution for 11 days; (b): XRD patterns of the surfaces of AF-Horizontal, 600-Horizontal, and 800-Horizontal specimens after weight loss test, revealing the formation of the Cu_2O phase.

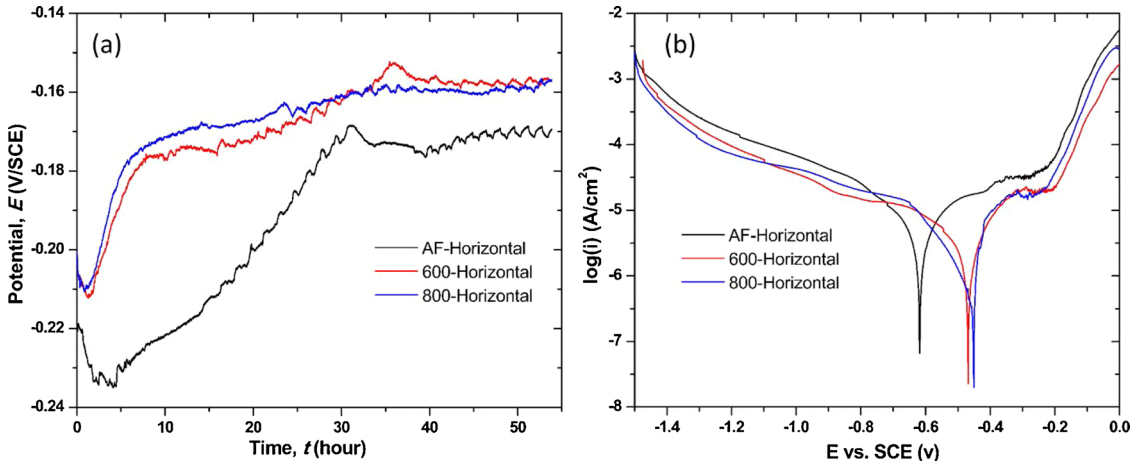

Fig. 10. (a): Open circuit potential vs. time curves of specimens in 3.5 wt.% NaCl water solution; (b): Potentiodynamic polarization test results, obtained after 1 h open-circuit immersion for AF-Horizontal, 600-Horizontal and 800-Horizontal specimens in 3.5 wt.% NaCl water solution.

Table 4
Corrosion test results obtained from potentiodynamic polarization measurements.

Specimen	E_{corr} (v)	i_{corr} (μA/cm^2)	i_p (μA/cm^2)	E_p (v)
AF-Horizontal	−0.620	7.586	31.623	−0.262
600-Horizontal	−0.468	3.388	21.380	−0.204
800-Horizontal	−0.451	3.236	16.218	−0.223

alloy with finer grains can have a higher rate of intergranular corrosion due to higher GBs density [52,53]. In addition, it has been reported that due to the possible intervention of GBs in passive layer formation, this passive layer can be less protective for specimens with finer grains, which in turn results in a higher corrosion rates [54,55]. Fig. 11(a) shows the surface of 800-Horizontal specimen after weight loss test. It is evident that intergranular corrosion attack occurred along grain boundaries, as indicated by the white arrows. In addition to intergranular corrosion, galvanic corrosion is another reason for the higher corrosion rate for the AF specimen. It's well known that a surface consisting of two phases can suffer from galvanic corrosion in a corrosive media where the more resistive phase serves as cathode and causes the corrosion of the other phase [56]. As mentioned before, AF specimens contain both α and δ phases, while VA specimens only contain the α phase. Studies have revealed that the δ phase exhibits a better corrosion resistance as compared to the α phase [20,21]. Consequently, the δ phase can work as a cathode and lead to preferred corrosion attacks on the α phase. Fig. 11(b) shows the surface morphology of AF specimen after corrosion test. Melt pool profiles are clearly observed, and the white structures are mainly distributed on regions close to melt pool borders, Fig. 11(c). It is clear that these white microstructures protrude out of the specimen surface, similar to etched microstructures shown in Fig. 3(d). Therefore, the observation of the white structures and dark regions can be ascribed to galvanic corrosion caused by the co-existence of α and δ phases.

4. Conclusions

Cu-10Sn alloy specimens have been successfully prepared with LPBF-AM. The effects of buliding direction and heat treatment on mechanical, thermal, and corrosion properties of Cu-10Sn alloy specimens are studied. The following conclusions are reached:

(1) The AF specimens under two different building orientations are found to have similar compression strength, thermal conductivity, and corrosion properties.
(2) The AF specimens have fine grains with an average grain size of ~2 μm, and consist of a Cu-rich α phase and a Sn-rich δ phase due to the rapid cooling during the LPBF-AM process. VA specimens possess equiaxed grains with significantly increased grain sizes. Only the α phase can be detected in VA specimens.
(3) The AF specimens exhibit a much higher compression strength than VA specimens due to the smaller grain size and the existence of inter-phase interfaces.
(4) Thermal conductivity of the AF specimens is ~10−20 % higher than that of 800 ℃ and 600 ℃ annealed specimens, which can be attributed to the high thermal-conductivity of the α phase in the AF specimens.

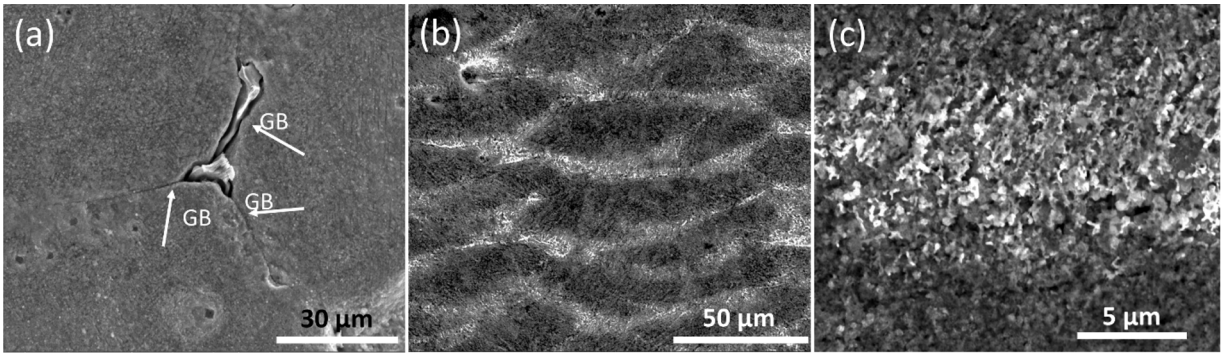

Fig. 11. SEM images of surface morphologies after weight loss test: (a) 800-Horizontal specimen showing intergranular corrosion; (b)/(c): AF-Horizontal specimen showing galvanic corrosion.

(5) Heat treatment results in a significant improvemnet in corrosion performance by decreasing the corrosion rate by almost 50 % due to the modification of passive layer morphology as well as the decrease of the susceptibility to intergranular corrosion and internal galvanic corrosion.

CRediT authorship contribution statement

Congyuan Zeng: Formal analysis, Investigation, Data curation, Visualization, Writing - original draft. **Bin Zhang:** Formal analysis, Investigation, Data curation, Visualization, Writing - original draft. **Ali Hemmasian Ettefagh:** Formal analysis, Investigation, Data curation, Writing - original draft. **Hao Wen:** Methodology, Validation, Investigation. **Hong Yao:** Methodology, Validation, Investigation. **W.J. Meng:** Writing - review & editing, Funding acquisition. **Shengmin Guo:** Conceptualization, Writing - original draft, Writing - review & editing, Supervision, Funding acquisition.

Declaration of Competing Interest

The authors declare that they have no known competing financial interests or personal relationships that could have appeared to influence the work reported in this paper.

Acknowledgements

This work is supported by the NSF EPSCoR award to the state of Louisiana to establish the Consortium for Innovation in Manufacturing and Materials (CIMM), grant number NSF #OIA-1541079. The use of instruments housed within the LSU Shared Instrumentation Facilities (SIF), a part of CIMM Core User Facilities (CUF), is acknowledged.

References

[1] K. Lee, C. Hu, K.-N. Tu, In situ scanning electron microscope comparison studies on electromigration of Cu and Cu (Sn) alloys for advanced chip interconnects, J. Appl. Phys. 78 (7) (1995) 4428–4437.
[2] B.S. Ünlü, E. Atik, Evaluation of effect of alloy elements in copper based CuSn10 and CuZn30 bearings on tribological and mechanical properties, J. Alloys. Compd. 489 (1) (2010) 262–268.
[3] A. Canakci, T. Varol, H. Cuvalci, F. Erdemir, S. Ozkaya, E. Yalcın, Synthesis of novel CuSn10-graphite nanocomposite powders by mechanical alloying, Micro Nano Lett. 9 (2) (2014) 109–112.
[4] X. Chen, Z. Wang, D. Ding, H. Tang, L. Qiu, X. Luo, G. Shi, Strengthening and toughening strategies for tin bronze alloy through fabricating in-situ nanostructured grains, Mater. Des. 66 (2015) 60–66 1980-2015.
[5] D.D. Gu, W. Meiners, K. Wissenbach, R. Poprawe, Laser additive manufacturing of metallic components: materials, processes and mechanisms, Int. Mater. Rev. 57 (3) (2012) 133–164.
[6] A.H. Ettefagh, C. Zeng, S. Guo, J. Raush, Corrosion behavior of additively manufactured Ti-6Al-4V parts and the effect of post annealing, Addit. Manuf. 28 (2019) 252–258.
[7] A.H. Ettefagh, S. Guo, Electrochemical behavior of AISI316L stainless steel parts produced by laser-based powder bed fusion process and the effect of post annealing process, Addit. Manuf. 22 (2018) 153–156.
[8] C.Y. Yap, C.K. Chua, Z.L. Dong, Z.H. Liu, D.Q. Zhang, L.E. Loh, S.L. Sing, Review of selective laser melting: materials and applications, Appl. Phys. Rev. 2 (4) (2015) 041101.
[9] Z. Mao, D.Z. Zhang, P. Wei, K. Zhang, Manufacturing feasibility and forming properties of Cu-4Sn in selective laser melting, Materials 10 (4) (2017) 333.
[10] A.P. Ventura, C.A. Wade, G. Pawlikowski, M. Bayes, M. Watanabe, W.Z. Misiolek, Mechanical properties and microstructural characterization of Cu-4.3 Pct Sn fabricated by selective laser melting, Metall. Mater. Trans. A 48 (1) (2017) 178–187.
[11] S. Scudino, C. Unterdörfer, K. Prashanth, H. Attar, N. Ellendt, V. Uhlenwinkel, J. Eckert, Additive manufacturing of Cu–10Sn bronze, Mater. Lett. 156 (2015) 202–204.
[12] C. Deng, J. Kang, T. Feng, Y. Feng, X. Wang, P. Wu, Study on the selective laser melting of CuSn10 powder, Materials 11 (4) (2018) 614.
[13] A. Bhat, V.K. Balla, S. Bysakh, D. Basu, S. Bose, A. Bandyopadhyay, Carbon nanotube reinforced Cu–10Sn alloy composites: mechanical and thermal properties, Mater. Sci. Eng. A 528 (22-23) (2011) 6727–6732.
[14] Z. Mao, D.Z. Zhang, J. Jiang, G. Fu, P. Zhang, Processing optimisation, mechanical properties and microstructural evolution during selective laser melting of Cu-15Sn high-tin bronze, Mater. Sci. Eng. A 721 (2018) 125–134.
[15] J. Wang, X. Zhou, J. Li, M. Brochu, Y.F. Zhao, Microstructures and properties of SLM-manufactured Cu-15Ni-8Sn alloy, Addit. Manuf. 31 (2020) 100921.
[16] Y.S. Touloukian, R. Powell, C. Ho, P. Klemens, Thermophysical properties of matter-the tprc data series. Volume 1. Thermal conductivity-metallic elements and alloys, Thermophysical and Electronic Properties Information Analysis Center, (1970).
[17] E. Sidot, N. Souissi, L. Bousselmi, E. Triki, L. Robbiola, Study of the corrosion behaviour of Cu–10Sn bronze in aerated Na2SO4 aqueous solution, Corros. Sci. 48 (8) (2006) 2241–2257.
[18] G. Ingo, T. De Caro, C. Riccucci, E. Angelini, S. Grassini, S. Balbi, P. Bernardini, D. Salvi, L. Bousselmi, M. Gener, Large scale investigation of chemical composition, structure and corrosion mechanism of bronze archeological artefacts from Mediterranean basin, Appl. Phys. A 83 (4) (2006) 513–520.
[19] C. Chiavari, A. Colledan, A. Frignani, G. Brunoro, Corrosion evaluation of traditional and new bronzes for artistic castings, Mater. Chem. Phys. 95 (2-3) (2006) 252–259.
[20] D. Šatović, L.V. Žulj, V. Desnica, S. Fazinić, S. Martinez, Corrosion evaluation and surface characterization of the corrosion product layer formed on Cu–6Sn bronze in aqueous Na2SO4 solution, Corros. Sci. 51 (8) (2009) 1596–1603.
[21] N. Souissi, E. Sidot, L. Bousselmi, E. Triki, L. Robbiola, Corrosion behaviour of Cu–10Sn bronze in aerated NaCl aqueous media–electrochemical investigation, Corros. Sci. 49 (8) (2007) 3333–3347.
[22] L. Robbiola, T. Tran, P. Dubot, O. Majerus, K. Rahmouni, Characterisation of anodic layers on Cu–10Sn bronze (RDE) in aerated NaCl solution, Corros. Sci. 50 (8) (2008) 2205–2215.
[23] K. Zohdy, M. Sadawy, M. Ghanem, Corrosion behavior of leaded-bronze alloys in sea water, Mater. Chem. Phys. 147 (3) (2014) 878–883.
[24] A. Drach, I. Tsukrov, J. DeCew, J. Aufrecht, A. Grohbauer, U. Hofmann, Field studies of corrosion behaviour of copper alloys in natural seawater, Corros. Sci. 76 (2013) 453–464.
[25] B. Zhang, Y. Song, G.Z. Voyiadjis, W.J. Meng, Assessing texture development and mechanical response in microscale reverse extrusion of copper, J. Mater. Res. 33 (8) (2018) 978–988.
[26] Y.M. Wang, T. Voisin, J.T. McKeown, J. Ye, N.P. Calta, Z. Li, Z. Zeng, Y. Zhang, W. Chen, T.T. Roehling, Additively manufactured hierarchical stainless steels with high strength and ductility, Nat. Mater. 17 (1) (2018) 63–71.
[27] Y. Zhong, L.-E. Rännar, S. Wikman, A. Koptyug, L. Liu, D. Cui, Z. Shen, Additive manufacturing of ITER first wall panel parts by two approaches: selective laser melting and electron beam melting, Fusion Eng. Des. 116 (2017) 24–33.
[28] M.M. Kirka, Y. Lee, D.A. Greeley, A. Okello, M.J. Goin, M.T. Pearce, R.R. Dehoff, Strategy for texture management in metals additive manufacturing, JOM 69 (3) (2017) 523–531.
[29] L. Thijs, K. Kempen, J.-P. Kruth, J. Van Humbeeck, Fine-structured aluminium products with controllable texture by selective laser melting of pre-alloyed AlSi10Mg powder, Acta Mater. 61 (5) (2013) 1809–1819.
[30] Y. Lu, S. Wu, Y. Gan, T. Huang, C. Yang, L. Junjie, J. Lin, Study on the microstructure, mechanical property and residual stress of SLM Inconel-718 alloy manufactured by differing island scanning strategy, Opt. Laser Technol. 75 (2015) 197–206.
[31] E. Hall, The deformation and ageing of mild steel: III discussion of results, Proc. Phys. Soc. Lond., Sect. B 64 (9) (1951) 747.
[32] Z. He, C. Jian, J.-C. Feng, Microstructure and mechanical properties of Ti6Al4V/Cu-10Sn bronze diffusion-bonded joint, Trans. Nonferrous Met. Soc. 19 (2009) s414–s417.
[33] E.A. Gadallah, M.A. Ghanem, M. Abd El-Hamid, A.E. El-Nikhaily, Effect of tin content and ECAP passes on the mechanical properties of Cu/Sn alloys, Am. J. Sci. Technol. 2 (1) (2014) 60.
[34] A.E. Nassef, A. Alateyah, M.A. El-Hadek, W. El-Garaihy, Mechanical behavior and fracture surface characterization of liquid-phase sintered Cu-Sn powder alloys, Adv. Mater. Lett. 8 (2017) 717–722.
[35] A. Nassef, M. El-Hadek, Microstructure and mechanical behavior of hot pressed Cu-Sn powder alloys, Adv. Mater. Sci. Eng. 2016 (2016).
[36] C. Zeng, H. Wen, H. Bellamy, P. Sprunger, P.J. Schilling, S. Guo, Titanium and nitrogen interactions under laser additive manufacturing conditions, Surf. Coat. Technol. 378 (2019) 124955.
[37] R. Abedinzadeh, S.M. Safavi, F. Karimzadeh, A study of pressureless microwave sintering, microwave-assisted hot press sintering and conventional hot pressing on properties of aluminium/alumina nanocomposite, J. Mech. Sci. Technol. 30 (5) (2016) 1967–1972.
[38] S. Pauly, P. Wang, U. Kühn, K. Kosiba, Experimental determination of cooling rates in selectively laser-melted eutectic Al-33Cu, Addit. Manuf. 22 (2018) 753–757.
[39] X. Wang, L.N. Carter, B. Pang, M.M. Attallah, M.H. Loretto, Microstructure and yield strength of SLM-fabricated CM247LC Ni-Superalloy, Acta Mater. 128 (2017) 87–95.
[40] N. Kurgan, Effect of porosity and density on the mechanical and microstructural properties of sintered 316L stainless steel implant materials, Mater. Des. 55 (2014) 235–241.
[41] D.S. Oh, Y.H. Kim, D. Ganbat, M.-H. Han, P. Lim, J.-H. Back, F.Y. Lee, H. Tawfeek, Bone marrow absorption and retention properties of engineered scaffolds with micro-channels and nano-pores for tissue engineering: a proof of concept, Ceram. Int. 39 (7) (2013) 8401–8410.
[42] N. Bekoz, E. Oktay, Mechanical properties of low alloy steel foams: dependency on porosity and pore size, Mater. Sci. Eng. A 576 (2013) 82–90.
[43] C.-L. Huang, Z.-Z. Lin, Y.-H. Feng, X.-X. Zhang, G. Wang, Thermal conductivity prediction of 2-dimensional square-pore metallic nanoporous materials with kinetic method approach, Int. J. Therm. Sci. 112 (2017) 263–269.
[44] A. Mallikarjunan, S. Sharma, S. Murarka, Resistivity of copper films at thicknesses

near the mean free path of electrons in copper minimization of the diffuse scattering in copper, Electrochem. Solid-State Lett. 3 (9) (2000) 437.
[45] J. Plombon, E. Andideh, V.M. Dubin, J. Maiz, Influence of phonon, geometry, impurity, and grain size on copper line resistivity, Appl. Phys. Lett. 89 (11) (2006) 113124.
[46] I. Sumirat, Y. Ando, S. Shimamura, Theoretical consideration of the effect of porosity on thermal conductivity of porous materials, J. Porous Mater. 13 (3-4) (2006) 439–443.
[47] C. Smith, Thermal Conductivity of Copper Alloys II.-COPPER-TIN Alloys III.-COPPER-PHOSPHORUS Alloys, AIME TECH PUBL, 1930, p. 11 1930.
[48] M. Cook, W. Tallis, The physical properties and annealing characteristics of standard phosphor-bronze alloys, J. Inst. Met. 67 (1941) 49–65.
[49] K. Pietrak, T.S. Wisniewski, A review of models for effective thermal conductivity of composite materials, J. Power Technol. 95 (1) (2015) 14.
[50] M. Booth, J. Brandon, R. Brizard, Ct. Chieh, W. Pearson, γ-Brasses with F cells, Acta Crystallogr, Sect. B: Struct. Crystallogr. Cryst. Chem. 33 (1) (1977) 30–36.
[51] S.I. Kim, K.H. Lee, H.A. Mun, H.S. Kim, S.W. Hwang, J.W. Roh, D.J. Yang, W.H. Shin, X.S. Li, Y.H. Lee, Dense dislocation arrays embedded in grain boundaries for high-performance bulk thermoelectrics, Science 348 (6230) (2015) 109–114.
[52] K. Ralston, N. Birbilis, C. Davies, Revealing the relationship between grain size and corrosion rate of metals, Scr. Mater. 63 (12) (2010) 1201–1204.
[53] S. Gollapudi, Grain size distribution effects on the corrosion behaviour of materials, Corros. Sci. 62 (2012) 90–94.
[54] W. Luo, C. Qian, X. Wu, M. Yan, Electrochemical corrosion behavior of nanocrystalline copper bulk, Mater. Sci. Eng. A 452 (2007) 524–528.
[55] A. Barbucci, G. Farne, P. Matteazzi, R. Riccieri, G. Cerisola, Corrosion behaviour of nanocrystalline Cu90Ni10 alloy in neutral solution containing chlorides, Corros. Sci. 41 (3) (1998) 463–475.
[56] N. Fu, X. Tang, D. Li, L. Parent, H. Tian, In situ investigation of local corrosion at interphase boundary under an electrochemical-atomic force microscope, J. Solid State Electrochem. 19 (2) (2015) 337–344.